An Artificial Skyrmion Platform with Robust Tunability in Synthetic Antiferromagnetic Multilayers

Yong Li, Qiyuan Feng, Sihua Li, Ke Huang, Mangyuan Ma, Weiliang Gan, Haibiao Zhou, Xiangjun Jin, Xiao Renshaw Wang, Yalin Lu, Wen Siang Lew,* Qingyou Lu,* and Fusheng Ma*

Magnetic skyrmions are topologically nontrivial spin structures, and their existence in ferromagnetically coupled multilayers has been widely reported with a disordered arrangement. Here, a nucleation scenario of ordered skyrmions in nanostructured synthetic antiferromagnetic (SAF) multilayers is proposed and experimentally demonstrated using direct magnetization imaging, indirect magnetometer and magnetoresistance measurement, and micromagnetic simulation. Instead of relying on Dzyaloshinskii–Moriya interaction, the antiferromagnetic interlayer exchange coupling in the SAF multilayers fulfills the role of nucleation and stabilization of skyrmions. The robustness of the proposed skyrmion nucleation scenario is examined against temperature from 4.5 to 300 K and device size from 400 to 1200 nm. Interestingly, these synthetic skyrmions still behave well with a size less than 100 nm. The higher stability than generic magnetic domains can be attributed to topological protection. The results thus provide an artificial skyrmion platform to meet the functional needs of high density and designable arrangement in magnonic and spintronic applications.

1. Introduction

Magnetic skyrmions, topologically protected quasi-particle with nontrivial spin configurations, are highly promising as an information carrier in next-generation spintronic devices for data storage and logic operation.[1–5] They have been firstly observed in noncentrosymmetric bulk magnetic materials at cryogenic temperatures[6–13] such as B20 compound MnSi, FeGe, and PdFe. Recently, stabilization of nanoscale skyrmions at room temperature (RT) were also experimentally realized in ultrathin Ir/Fe,[14] Ta/CoFeB/MgO,[15] Ta/CoFeB/TaO,[15] Pt/Co,[16,17] Ir/Co/Pt,[17] Pt/Co/MgO,[18] Ir/Fe/Co/Pt,[19] and IrMn/CoFeB[20] multilayer films. In these multilayers, the heavy-metal spacing layers provide an asymmetric Dzyaloshinskii–Moriya interaction (DMI)[21,22] at the ferromagnet/heavy-metal interface at the expense of interlayer exchange coupling (IEC). Although the presence of interfacial DMI stabilizes the existence of skyrmion, the nucleation is random resulting in a disordered arrangement. It has been demonstrated that the spin texture of skyrmions in multilayers are nonidentical for all the individual magnetic layers and cannot be effectively described as a 2D "ML" spin texture as shown in **Figure 1**a.[23,24] On the other hand, artificially periodic arrangements of skyrmions in 1D or 2D provide a novel type of "Metamaterial," i.e., skyrmion-based magnonic crystals (SBMCs),[25–28] in which the magnetization can be periodically modulated by ordered skyrmion lattices. In comparison with lithographically patterned magnonic crystals, a strong advantage of SBMCs is that the propagation of spin waves

Y. Li, M. Ma, X. Jin, Prof. F. Ma
Jiangsu Key Laboratory of Opto-Electronic Technology
Center for Quantum Transport and Thermal Energy Science
School of Physics and Technology
Nanjing Normal University
Nanjing 210046, China
E-mail: phymafs@njnu.edu.cn
Dr. Q. Feng, Dr. H. Zhou, Prof. Y. Lu, Prof. Q. Lu
Anhui Province Key Laboratory of Condensed
Matter Physics at Extreme Conditions
High Magnetic Field Laboratory
Chinese Academy of Sciences
Hefei 230031, China
E-mail: qxl@ustc.edu.cn

Dr. Q. Feng, Dr. H. Zhou, Prof. Y. Lu, Prof. Q. Lu
Hefei National Laboratory for Physical Sciences at the Microscale
University of Science and Technology of China
Hefei 230026, China
Dr. S. Li, K. Huang, W. Gan, Prof. X. Renshaw Wang, Prof. W. S. Lew
School of Physical and Mathematical Sciences
Nanyang Technological University
21 Nanyang Link, Singapore 637371, Singapore
E-mail: wensiang@ntu.edu.sg
Prof. X. Renshaw Wang
School of Electrical and Electronic Engineering
Nanyang Technological University
50 Nanyang Ave, Singapore 639798, Singapore
Prof. Q. Lu
Anhui Laboratory of Advanced Photon Science and Technology
University of Science and Technology of China
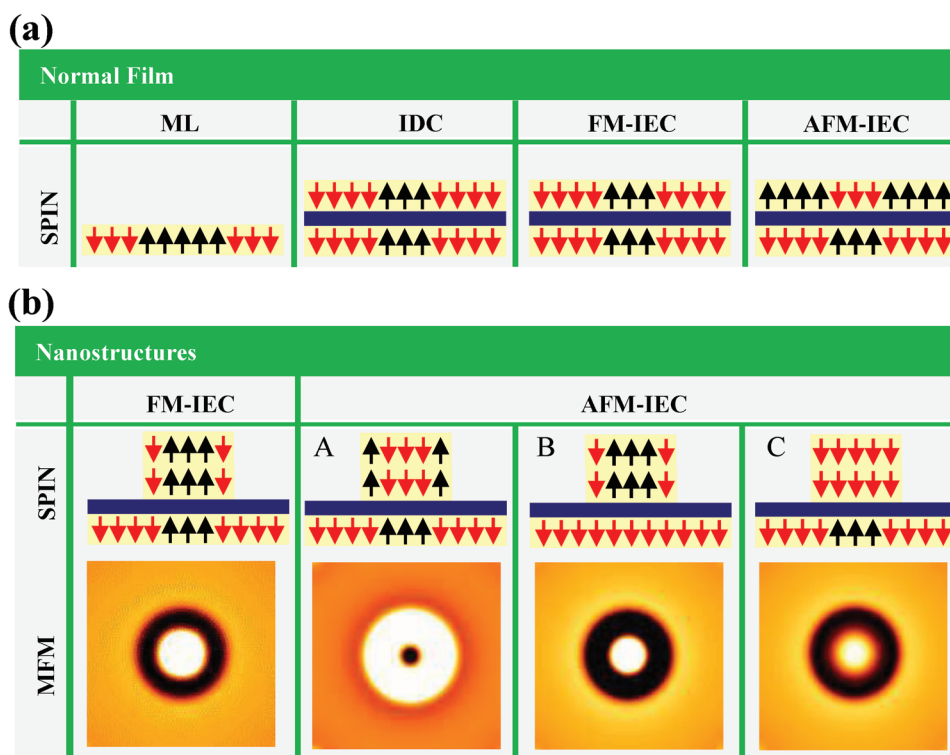Hefei 230026, China

Figure 1. Cross-sections of skyrmion spin textures along the radial directions in a) single- and multilayer magnetic thin films and b) top-layer-nanostructured SAF multilayers (the upper panel). The black/red arrows represent the out-of-plane magnetization is up/down. The corresponding simulated MFM images of skyrmion in nanostructured SAF multilayers are shown in the lower panel of (b).

inside can be dynamically manipulated by simply reconfiguring the property of skyrmions.[25] Furthermore, SBMCs are suitable candidates for topological matter investigation, such as the realization of topological magnonic insulators.[26–28] However, the realization of SBMCs is restricted by the random nucleation of skyrmion in magnetic multilayers with interfacial DMI.[15–19] One route to realize ordered skyrmion arrangement, which allows for high/flexible tunability and exploits artificial skyrmions, have recently been proposed and realized at RT.[29–38] These artificial skyrmions are realized by imprinting the magnetic vortex of the top nanodots into the underlayer film with perpendicular magnetic anisotropy without the requirement of DMI. Although the arrangement of skyrmion can be flexibly designed by nanopatterning the top nanodots, the skyrmion size cannot be adjusted as they are geometrically limited by the size of the top nanodots. Therefore, a skyrmion platform, showing designable arrangement and size tunability simultaneously, is still missing.

In this work, we propose and experimentally demonstrate the nucleation of artificial skyrmions in top-layer-nanostructured synthetic antiferromagnetic (SAF) multilayers, in which the antiferromagnetic interlayer exchange coupling (AFM-IEC) between the top nanodots and the film beneath gives rise to the nucleation and stabilization of skyrmions without requiring of DMI. The synthetic skyrmion formation process is directly characterized by magnetic force microscopy (MFM) imaging, and further confirmed by the magnetometer and magnetoresistance measurements as well as micromagnetic simulations. In contrast to the reported artificial skyrmions,[29–37] we find

that, once nucleated, the size of AFM-IEC induced skyrmion will not be geometrically limited and can be widely adjusted to a size much smaller than that of the top nanodots. Furthermore, the robustness of the skyrmion nucleation mechanism against temperature from 4.5 to 300 K and device size from 400 to 1200 nm are also examined. The demonstrated synthetic skyrmion system provides a readily designable platform for prospective materials based on ordered skyrmion arrangement.

2. Proposed Model

Considering a symmetric ferromagnet/nonmagnet/ferromagnet trilayer film, the two ferromagnetic layers can effectively interact via either interlayer dipolar coupling (IDC) or IEC depending on the thickness of the nonmagnetic spacing layer.[17,39] From the cross-sections of skyrmion spin textures along the radial directions as shown in Figure 1a, the IDC[15–19] and ferromagnetic interlayer exchange coupling (FM-IEC)[36,40–42] stabilize hybrid skyrmions with the same topology; while the AFM-IEC nucleates skyrmions of opposite topology charges.[43] The situation becomes even more complex for nonsymmetric ferromagnet/nonmagnet/ferromagnet trilayer film with its top ferromagnetic layer patterned into circular dots as the cross-sections shown in Figure 1b. From the cross-sections of skyrmion spin textures along the radial directions of the top circular dots, the FM-IEC stabilizes skyrmion-like spin textures across both the top dot and bottom film as reported.[36,44,45] Here, we consider a noncompensated

SAF multilayer with AFM-IEC. As shown in Figure 1b, there are three possible AFM-IEC induced skyrmion nucleation scenarios: Type AFM-IEC-A, skyrmions exist in both the top dot and the bottom film but with opposite topology charges; Type AFM-IEC-B, skyrmion exists only in the top dot; Type AFM-IEC-C, skyrmion exists only in the bottom film beneath the top dot. These three types of skyrmions can be distinguished from their corresponding MFM images as simulated in Figure 1b.

3. Experimental Results

To experimentally demonstrate the type of the proposed AFM-IEC skyrmions, the used multilayers are magnetron-sputtered in the noncompensated form of Ta(4)/Pt(4)/[Pt(0.6)/Co(0.6)]$_2$/Ru(0.9)/[Co(0.6)/Pt(0.6)]$_4$/Ta(4) (the number in parentheses are nominal thickness in nanometer, and indicated as [Pt/Co]$_2$/Ru/[Co/Pt]$_4$). For reference, three Ta(4)/Pt(4)/[Pt(0.6)/Co(0.6)]$_n$/Ta(4) multilayers (n = 2, 4, and 6) were prepared. The magnetization reversal properties of the [Pt/Co]$_2$/Ru/[Co/Pt]$_4$ multilayers and the reference [Co/Pt]$_n$ multilayers display multi- and single-step switching, respectively, see Figure S1 in the Supporting Information. The out-of-plane magnetization hysteresis (M–H) loop of the [Pt/Co]$_2$/Ru/[Co/Pt]$_4$ multilayers exhibits a typical character of synthetic antiferromagnetic multilayers with the presence of AFM-IEC. The top [Co/Pt]$_4$ layer was patterned into circular dots of different diameters ranging from 400 to 1200 nm. In such a half-etched structure, the bottom continuous [Pt/Co]$_2$ film can be divided into two regions: one is the non-dot-covered region behaving as continuous ferromagnetic films; the other one is the dot-covered region interacting with the circular dot on its top via AFM-IEC. These two regions exhibit different magnetization switching behaviors.

To verify the existence of skyrmions, we first performed the real-space imaging using home-built MFM at RT. The MFM measurement was carried out with an out-of-plane magnetic field varying from 12 to −12 kOe. **Figure 2**a shows the historical changing of the magnetic morphology of the nanostructured SAF multilayers at selected fields. The diameters of the top [Co/Pt]$_4$ circular dots changes from 400 nm (first row) to 1200 nm (fifth row) with an interval of 200 nm. Their physical properties can be found from the scanning electron microscope (SEM) images shown in Figure S2 in the Supporting Information. As the magnetic field swept from 12 to −12 kOe, the magnetization changed from positively saturated state to nonsaturated state and then to negatively saturated state. Interestingly, in the nonsaturated state, the dot-covered regions exhibit a historical magnetization morphology, which highly depend on the magnetic fields and the size of the top circular dots. Generally, the dot-covered regions exhibit a brighter color and shrinks inward until eventually annihilated with field decreasing. This phenomenon is consistent for dots of various sizes as indicated by dashed circles in Figure 2a. For instance, at the second row of Figure 2a, the center brighter region shrinks from the geometrical size of the top dot to a much
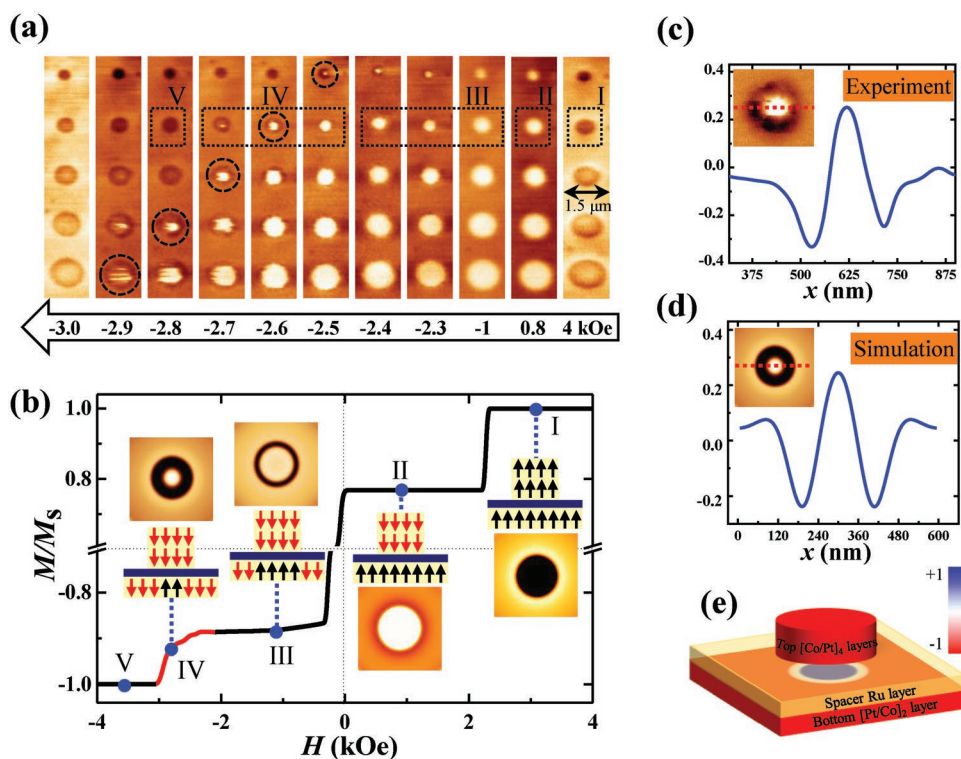

Figure 2. a) Measured room temperature MFM images of nanostructured SAF multilayer (diameters of top dots: 400, 600, 800, 1000, and 1200 nm) at selected fields starting from positive saturation. b) Simulated M–H loop of nanostructured SAF multilayer with a top dot diameter of 400 nm. The insets show cross-sections of spin textures along the radial directions and the corresponding simulated MFM images at typical fields. Line cut along the dot radial direction of the c) measured (as labeled by the dashed circle in (a)) and d) simulated MFM images (as the inset at stage IV). e) Diagram of synthetic skyrmion configuration at stage IV as labeled in (b).

**ADVANCED
SCIENCE NEWS**

www.advancedsciencenews.com

**ADVANCED
FUNCTIONAL
MATERIALS**

www.afm-journal.de

smaller value when the field decreases from −2.5 to −2.7 kOe. This observation is different from the reported artificial skyrmion, whose sizes cannot be adjusted and limited by the geometrical size of the top dot.[29–37]

To understand the measured MFM images corresponding to which type of AFM-IEC skyrmions, we performed micromagnetic simulations to calculate the M–H loops, spin textures, and MFM images of nanostructured SAF multilayer with a top dot of diameter 400 nm as shown in Figure 2b. By analyzing the spin textures as the field decreasing from +6 to −6 kOe, see insets in Figure 2b, we can clearly understand the whole magnetization reversal process by dividing the simulated M–H loop into 5 stages. At stage I, the external field is larger enough to saturate both the top dot and the bottom film. At stage II, the AFM-IEC between the top dot and the dot-covered region can overcome the external field resulting in the switching of the top dot. At stage III, the non-dot-covered region of the bottom film is switched by the reversed external field, however, the AFM-IEC protects the dot-covered region from external field induced switching. At stage IV, the dot-covered region starts to shrink as the negatively increasing field gradually offset the AFM-IEC protection. At stage V, the dot-covered region is fully switched, and both the top dot and the bottom film are negatively saturated. Therefore, considering the whole bottom film, a skyrmion-like spin texture can nucleate during the field-induced magnetization reversal process at both the stage III and the stage IV with the assistance of the AFM-IEC between the top dot and the bottom dot-covered region. The skyrmion at stage III has fixed size limited by the geometry of the top dot, which is similar to the reported artificial skyrmions.[29–37] In contrast, the size of skyrmion at stage IV can be adjusted by changing external field and can be smaller than 100 nm. To find out the transition manner of spin from the center of skyrmion to the surrounding, we numerically simulated the spin configuration of the bottom layer at stage III to stage IV as shown in Figure S3 in the Supporting Information. It is found that the skyrmions are Néel type. By comparing the measured and simulated historical MFM images, the states marked by five dashed rectangles at the second row of Figure 2a are one-to-one matched with the simulated stages as indicated in Figure 2b. Therefore, we can preliminarily confirmed that the experimentally observed white spots in the MFM images indicate the successful appearance of AFM-IEC induced skyrmion. To further clarify the type of AFM-IEC skyrmions (A, B, or C in Figure 1b), we did a line-cut along the dot radial direction (red dash line) of the measured (marked by dashed circle at the
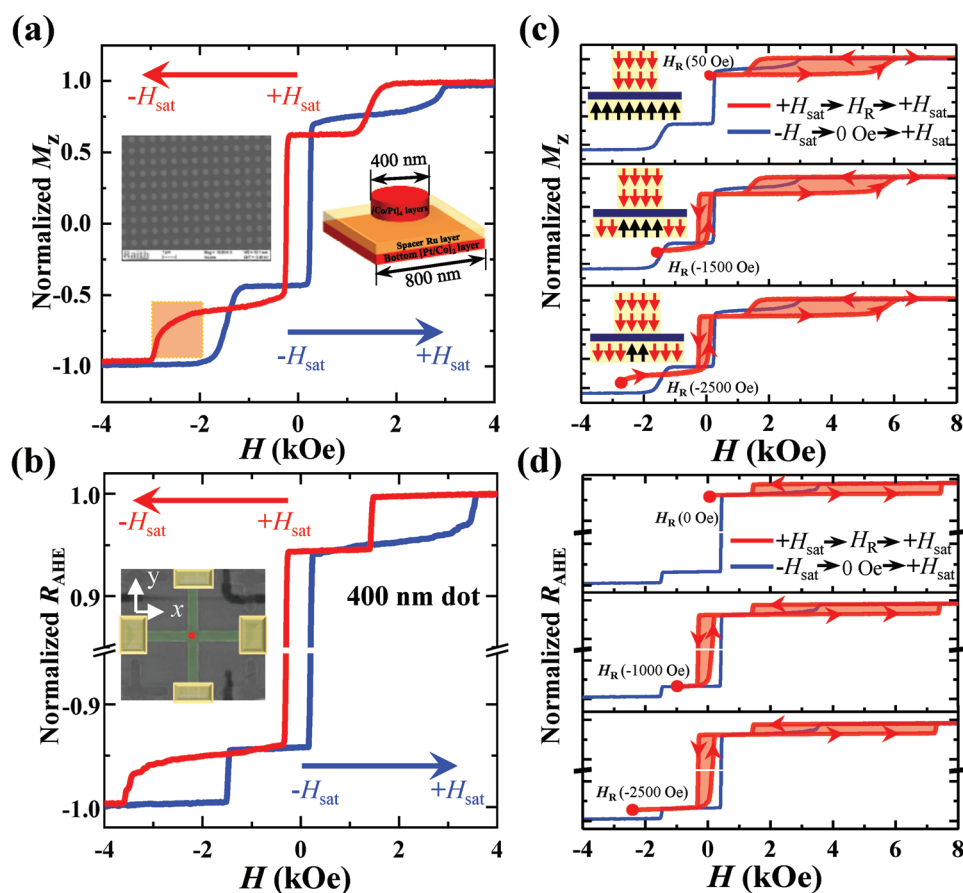

Figure 3. a) Normalized out-of-plane M–H loop of nanostructured SAF multilayer with a top dot diameter of 400 nm measured by Kerr microscopy at room temperature. Insert (left) is the SEM image of nanostructured SAF multilayer with a 2D arrangement of the top 400 nm dot in a square lattice. Insert (right) is the schematic of one unit cell. b) Normalized R_{AHE}–H loops of cross-structured SAF multilayer with a top dot diameter of 400 nm by magnetoresistance measurement. Inset is the SEM image of the cross-structured SAF multilayer. The normalized minor M–H and R_{AHE}–H loops are shown in c,d). Blue/red lines indicate the major/minor loops and insets are the corresponding spin textures at selected reversal fields H_R.

**ADVANCED
SCIENCE NEWS**

www.advancedsciencenews.com

**ADVANCED
FUNCTIONAL
MATERIALS**

www.afm-journal.de

first row of Figure 2a) and simulated (stage IV in Figure 2b) MFM images as shown in Figure 2c,d, respectively. The simulated MFM images were obtained with a tip height of 50 nm with the best agreement with experimental MFM images. The simulated MFM images of different tip heights can be found from Figure S4 in the Supporting Information. It is found that there is a good consistency between the measured and simulated MFM images in Figure 2c,d. In additional, the consistency was further confirmed by comparing the simulated and measured MFM images at different typical magnetization states under various external fields as shown in Figure S5 in the Supporting Information. Hence, we can conclude that the observed skyrmion is the type AFM-IEC-C as schematically shown in Figure 2e. In the view of their size tunability, the AFM-IEC-C skyrmions provides a stronger coherent interaction between the top [Co/Pt]$_4$ dot and the beneath [Pt/Co]$_2$ film than that by IDC.[44,46] For comparison, we also did the MFM measurement on fully etched SAF multilayers, i.e., both the top and bottom layers are patterned into a circular dot. However, the measured MFM images do not exhibit magnetization morphology of AFM-IEC skyrmions as shown in Figure S6 in Supporting Information.

The nucleation scenario of AFM-IEC-C skyrmions has been demonstrated by direct MFM imaging. We also employ two indirect methods to confirm the MFM observations: $M–H$ loop measurement by a polar magneto-optical Kerr effect (MOKE) technique and anomalous Hall effect (AHE) measurements by 4-point magneto-transport technique. **Figure 3**a,b are the measured $M–H$ and AHE resistance hysteresis ($R_{AHE}–H$) loops of nanostructured SAF multilayers with a top dot diameter of 400 nm at RT, respectively. For the $M–H$ loops measurement, a 2D arrangement of 400 nm dots in a square lattice with a period of 800 nm was prepared as the inserted SEM images and schematic of one unit cell in Figure 3a. Consistent with the simulated $M–H$ loop in Figure 2b, the optically measured $M–H$ loop also exhibits five magnetization stages, in which the AFM-IEC skyrmion stage is highlighted. Besides measuring major $M–H$ loops, we also carried out the measurement of minor $M–H$ loops, in which the field decreases from a positively saturated value $+H_{sat}$ to a selected reversal field H_R ($|H_R| < |H_{sat}|$) and then back to $+H_{sat}$. The selected H_R (50, −1500, and −2500 Oe) correspond to magnetization states of different spin textures (stage II, stage III, and stage IV) as seen from the insets in Figure 3c. It is clearly found that the minor loops exhibit an irreversible magnetization process. For the conditions of $H_R = −2500$ and −1500 Oe, the bottom layer is first saturated by external field through skyrmion expanding and reach the spin texture state at $H_R = 50$ Oe. For $H_R = 50$ Oe, the AFM-IEC protects the top dot from saturating by the external field and resulting in a much higher saturation field $+H_{sat}$ than that of the major loop. This irreversible magnetization process also indicates that the spin texture at stage II is a purely AFM state (top dot and bottom film are fully saturated in opposite directions) rather than an AFM-IEC-C skyrmion. If the spin texture at stage II is in the form of AFM-IEC-C skyrmion, the minor reversal loop will consistent with the major loop as schematically explained in Figure S7 (Supporting Information). Figure 3b/d is the measured major/minor $R_{AHE}–H$ loops of the nanostructured SAF multilayer with a top dot of diameter 400 nm at RT. The bottom

[Pt/Co]$_2$ layer was fabricated into cross bar with a bar width of 3 μm, and the top [Co/Pt]$_4$ layer was patterned into a circular dot of diameter 400 nm located at the center of the cross bar. It is found that the measured R_{AHE} behaves in a similar manner to the optically measured magnetization. Hence, both the $M–H$ and $R_{AHE}–H$ loop measurements can act as an indirect method to characterize the presence of AFM-IEC-C skyrmion.

So far, we have mainly focused on the demonstration of creating AFM-IEC-C skyrmions at RT by patterning the top layer of the SAF multilayers into a circular dot with fixed diameter of 400 nm. To exam the generality and robustness of the scenario, we expand the investigation to various dot-sizes and temperatures. Actually, the AFM-IEC-C skyrmions nucleated in different field ranges depending on the size of the top dots as indicated by the five rows in Figure 2a. **Figure 4**a shows the optically measured $M–H$ loops with top dots of diameters 200, 300, 400, and 600 nm arranged in a square lattice. It is found that the saturation field and skyrmion existing field range increase slightly with dot size increasing, while the switching field of the bottom layer decreases. To investigate the effect from the arranging manner of the top dots, we also patterned the top dots into a honeycomb lattice. There is no difference between the $M–H$ loops of the top dots arranged into square and honeycomb lattices. Figure 4b shows the $R_{AHE}–H$ loops for top dots of three diameters (200, 300, and 400 nm). A similar phenomenon
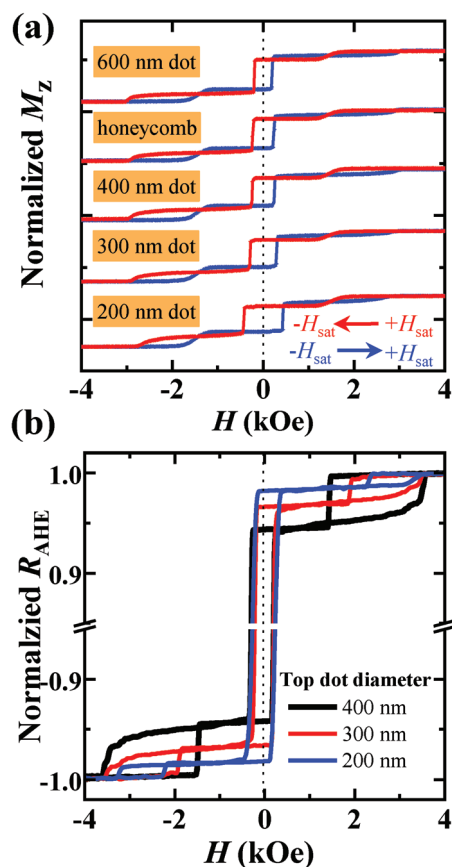

Figure 4. Normalized out-of-plane a) $M–H$ loops and b) $R_{AHE}–H$ loops of nanostructured SAF films with top dots of various diameters measured at RT.

1907140 (5 of 8)

**ADVANCED
SCIENCE NEWS**

www.advancedsciencenews.com

**ADVANCED
FUNCTIONAL
MATERIALS**

www.afm-journal.de

to M–H loops is observed that the top dot size slightly affect the skyrmion existing field range. The skyrmion annihilation field or the saturation field decreases as dot size decreases. Therefore, comprehensively considering the MFM images in Figure 2a, the M–H and R_{AHE}–H loops in Figure 4, the nucleation of AFM-IEC-C skyrmion is robust against the size of the top dot with a slight variation of the skyrmion existing field range.

From the application point of view, the temperature-dependent stability is also an important factor, particularly for spintronic space devices. To exam the thermal stability of nucleating AFM-IEC-C skyrmions, the low temperature R_{AHE}–H loops and MFM measurements were performed from 4.5 to 300 K. **Figure 5**a shows the fraction of the R_{AHE}–H loops corresponding to the skyrmion existing field range for the top dot of 400 nm diameter, it is found that the skyrmion existing field ranges (from the starting of stage III to the annihilation of stage

IV) increase to higher fields with temperature decreasing. The temperature dependence of the skyrmion existing fields is more clearly described in the field-temperature diagram as shown in Figure 5b. This phase diagram is extracted from the measured MFM images at 4.5, 100, 200, and 300 K for the top dot of 400 nm diameter as shown in Figures 5c–e and 2a, respectively. The MFM images of the top dot with various sizes measured at room temperature and low temperatures with a smaller field interval can be found in Figure S8 in Supporting Information. For easily understanding, we divide the diagram into three phases corresponding to the stages in Figure 2b: stage III, stage IV, and stage V. It is found that the stage IV moves to higher fields (also see dashed circles in Figure 5c–e) and becomes broader at lower temperatures. Together with the observation from the temperature-dependent R_{AHE}–H loops, this can be understood from the enhancement of the AFM-IEC strength of the

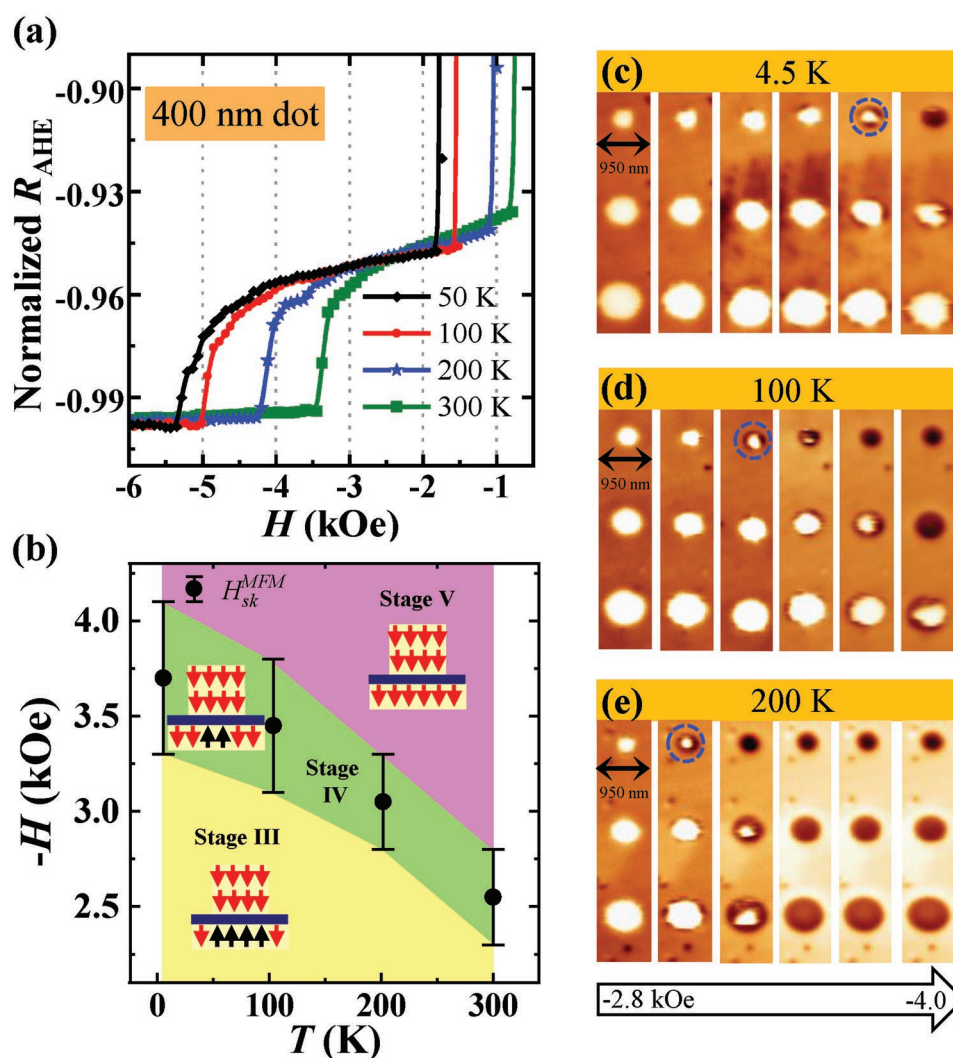**Figure 5.** a) Fraction of the measured R_{AHE}–H loops of nanostructured SAF film with a top dot of diameter 400 nm at various temperatures. b) Field-temperature magnetization phase diagrams of nanostructured SAF film with a top dot of diameter 400 nm derived from the MFM measurements. The phase diagram divided into three phases corresponding to three stages: stage III (skyrmion size is equal to the physical size of the top dot), stage IV (skyrmion size is smaller than the physical size of the top dot), and stage V (saturated along external field). Insets are the cross-sections of spin textures along the top dot radial directions. Low-temperature MFM images measured at c) 4.5 K, d) 100 K, and e) 200 K for the top dots with diameters of 400, 600, and 800 nm, respectively.

SAF multilayers at a lower temperature as shown in Figure S9 in Supporting Information.[47]

4. Conclusion

We proposed an artificial skyrmion platform in nanostructured synthetic antiferromagnetic multilayers. The antiferromagnetic interlayer exchange coupling assisted skyrmion nucleation process has been experimentally demonstrated via direct magnetization imaging and indirect detection by magneto-optical and electron-transport technology as well as micromagnetic simulations. In contrast to the reported artificial skyrmions, our AFM-IEC skyrmions exhibit a highly shrinking/expanding tunability and can break away from geometry limit. The skyrmion nucleation scenario is robust to dimension, temperature, and external magnetic field. Our demonstrated AFM-IEC skyrmions greatly enrich the flexibility of skyrmionic devices and provide a synthetic material platform for designing functional magnonic and spintronic structures based on ordered skyrmion arrangement, i.e., data storage, neuromorphic computing, and microwave oscillators applications.

5. Experimental Section

Sample Preparation: The synthetic antiferromagnetic multilayers Ta(4)/Pt(4)/[Pt(0.6)/Co(0.6)]$_2$/Ru(0.9)/[Co(0.6)/Pt(0.6)]$_4$/Ta(4) were deposited on the thermally oxidized silicon wafer use DC magnetron sputtering technique at room temperature. Argon gas ($\approx$2.3 $\times$ 10^{-3} Torr) was used during the sputtering process with a background pressure of 2 $\times$ 10^{-8} Torr, and the deposition rates for Pt, Co, and Ru were 0.14, 0.21, and 0.10 Å s^{-1}, respectively. In the SAF multilayers, the bottom [Pt(0.6)/Co(0.6)]$_2$ layer and the top [Co(0.6)/Pt(0.6)]$_4$ layer are antiferromagnetically coupled through the Ru spacer layer via interlayer exchange coupling. The SAF multilayers were patterned via electron beam lithography and Ar$^+$ ion milling methods. For MFM imaging and Kerr measurement, the top [Co(0.6)/Pt(0.6)]$_4$ layer was patterned into 2D arrays of circular nanodots of various diameters from 400 to 1200 nm. To measure the anomalous hall resistance, the bottom [Pt(0.6)/Co(0.6)]$_2$ layer was patterned into cross bar (length 40 μm and width 3 μm), while the top [Co(0.6)/Pt(0.6)]$_4$ layer was patterned into a single circular dot of various diameters (200, 300, and 400 nm) and located at the center of the cross bar.

Magneto Optic Kerr Effect Microscopy: The MagVision Kerr microscopy system operating in polar mode was used to measure the out-of-plane magnetization hysteresis (both major and minor) loops. An ultrabright 525 nm light source allowed for data capture rates up to 60 Hz. Please refer to https://www.vertisis.com.sg/.

Magnetic Force Microscopy: The magnetization imaging were performed using a home-built variable temperature MFM, equipped with a 20 T superconducting magnet.[48,49] A commercial piezoresistive cantilever (PRC400; Hitachi High-Tech Science Corporation) was incorporated as the force sensor. The resonant frequency of the cantilever is about 42 kHz. The MFM tip has a magnetic coating consisting of 5 nm Cr, 50 nm Fe, and then 5 nm Au films. This magnetic coating was magnetized perpendicular to the cantilever. The magnetic coercivity and saturation fields are $\approx$250 and $\approx$2000 Oe, respectively. A built-in phase-locked loop (R9 controller; RHK Technology) was utilized for MFM scanning control and signal processing. MFM images were collected in a constant height mode. First, a topographic image was obtained using contact mode, from which the sample surface tilting along the fast and slow scan axes could be compensated. Then the tip was lifted by $\approx$100 nm to the surface and MFM images were obtained in frequency-modulation mode.

Anomalous Hall Resistance Measurement: The out-of-plane R_{AHE}–H loops were determined by applying a 21 Hz 100 μA square wave current from a sourcemeter (keithley 6221) and measuring the voltage at each maximum and minimum value with a multimeter (keithley 2182A). The results can also be produced with DC current, however, the signals are much more noisy as shown in Figure S10 (Supporting Information). The out-of-plane magnetic field was supplied by the Oxford TeslatronPT, and the working temperature can change from 2 to 300 K.

Micromagnetic Simulations: The micromagnetic simulation was carried out using the commercial Landau–Lifschitz–Gilbert (LLG) Micromagnetic Simulator software.[50] The simulated structure has a volume of 3 μm $\times$ 3 μm $\times$ 4 nm: a bottom magnetic layer of 1 nm, a middle nonmagnetic layer of 1 nm, and a top magnetic layer of 2 nm. The top magnetic layer was simulated in the form of circular dot of various diameters. The cell size is 5 nm $\times$ 5 nm $\times$ 1 nm. The used material parameters were saturation magnetization: M_s = 1020 emu cm^{-3}; exchange constant A = 1.05 $\times$ 10^6 erg cm^{-1}; perpendicular magnetic anisotropy constant K_u = 7.6 $\times$ 10^6 erg cm^{-3}; interlayer exchange coupling strength J_{iec} = −0.4 erg cm^{-2}. The MFM images with different tip heights were calculated from the simulated equilibrium magnetization at selected external magnetic fields.

Supporting Information

Supporting Information is available from the Wiley Online Library or from the author.

Conflict of Interest

The authors declare no conflict of interest.

**ADVANCED
SCIENCE NEWS**

www.advancedsciencenews.com

**ADVANCED
FUNCTIONAL
MATERIALS**

www.afm-journal.de

[1] N. Nagaosa, Y. Tokura, *Nat. Nanotechnol.* **2013**, *8*, 899.

[2] R. Wiesendanger, *Nat. Rev. Mater.* **2016**, *1*, 16044.

[3] A. Fert, N. Reyren, V. Cros, *Nat. Rev. Mater.* **2017**, *2*, 17031.

[4] W. Jiang, G. Chen, K. Liu, J. Zang, S. G. E. te Velthuis, A. Hoffmann, *Phys. Rep.* **2017**, *704*, 1.

[5] X. Zhang, Y. Zhou, K. M. Song, T-E. Park, J. Xia, M. Ezawa, X. Liu, W. Zhao, G. Zhao, S. Woo, **2019**, arXiv:1906.04718.

[6] A. Neubauer, C. Pfleiderer, B. Binz, A. Rosch, R. Ritz, P. G. Niklowitz, P. Böni, *Phys. Rev. Lett.* **2009**, *102*, 186602.

[7] M. C. Langner, S. Roy, S. K. Mishra, J. C. T. Lee, X. W. Shi, M. A. Hossain, Y.-D. Chuang, S. Seki, Y. Tokura, S. D. Kevan, R. W. Schoenlein, *Phys. Rev. Lett.* **2014**, *112*, 167202.

[8] S. X. Huang, C. L. Chien, *Phys. Rev. Lett.* **2012**, *108*, 267201.

[9] S. Mühlbauer, B. Binz, F. Jonietz, C. Pfleiderer, A. Rosch, A. Neubauer, R. Georgii, P. Böni, *Science* **2009**, *323*, 915.

[10] X. Z. Yu, Y. Onose, N. Kanazawa, J. H. Park, J. H. Han, Y. Matsui, N. Nagaosa, Y. Tokura, *Nature* **2010**, *465*, 901.

[11] S. Seki, X. Z. Yu, S. Lshiwata, Y. Tokura, *Science* **2012**, *336*, 198.

[12] X. Z. Yu, N. Kanazawa, Y. Onose, K. Kimoto, W. Z. Zhang, S. Ishiwata, Y. Matsui, Y. Tokura, *Nat. Mater.* **2011**, *10*, 106.

[13] N. Romming, C. Hanneken, M. Menzel, J. E. Bickel, B. Wolter, K. von Bergmann, A. Kubetzka, R. Wiesendanger, *Science* **2013**, *341*, 636.

[14] S. Heinze, K. von Bergmann, M. Menzel, J. Brede, A. Kubetzka, R. Wiesendanger, G. Bihlmayer, S. Blügel, *Nat. Phys.* **2011**, *7*, 713.

[15] W. Jiang, P. Upadhyaya, W. Zhang, G. Yu, M. B. Jungfleisch, F. Y. Fradin, J. E. Pearson, Y. Tserkovnyak, K. L. Wang, O. Heinonen, S. G. E. te Velthuis, A. Hoffmann, *Science* **2015**, *349*, 283.

[16] S. Woo, K. Litzius, B. Krüger, M.-Y. Im, L. Caretta, K. Richter, M. Mann, A. Krone, R. M. Reeve, M. Weigand, P. Agrawal, I. Lemesh, M.-A. Mawass, P. Fischer, M. Kläui, G. S. D. Beach, *Nat. Mater.* **2016**, *15*, 501.

[17] C. Moreau-Luchaire, C. Moutafis, N. Reyren, J. Sampaio, C. A. F. Vaz, N. Van Horne, K. Bouzehouane, K. Garcia, C. Deranlot, P. Warnicke, P. Wohlhüter, J.-M. George, M. Weigand, J. Raabe, V. Cros, A. Fert, *Nat. Nanotechnol.* **2016**, *11*, 444.

[18] O. Boulle, J. Vogel, H. Yang, S. Pizzini, D. de Souza Chaves, A. Locatelli, T. O. Menteş, A. Sala, L. D. Buda-Prejbeanu, O. Klein, M. Belmeguenai, Y. Roussigné, A. Stashkevich, S. M. Chérif, L. Aballe, M. Foerster, M. Chshiev, S. Auffret, I. M. Miron, G. Gaudin, *Nat. Nanotechnol.* **2016**, *11*, 449.

[19] A. Soumyanarayanan, M. Raju, A. L. G. Oyarce, A. K. C. Tan, M.-Y. Im, A. P. Petrovic, P. Ho, K. H. Khoo, M. Tran, C. K. Gan, F. Ernult, C. Panagopoulos, *Nat. Mater.* **2017**, *16*, 898.

[20] G. Yu, A. Jenkins, X. Ma, S. A. Razavi, C. He, G. Yin, Q. Shao, Q. L. He, H. Wu, W. Li, W. Jiang, X. Han, X. Li, A. C. Bleszynski Jayich, P. K. Amiri, K. L. Wang, *Nano Lett.* **2018**, *18*, 980.

[21] I. Dzyaloshinsky, *J. Phys. Chem. Solids* **1958**, *4*, 241.

[22] T. Moriya, *Phys. Rev. Lett.* **1960**, *4*, 228.

[23] W. Li, I. Bykova, S. Zhang, G. Yu, R. Tomasello, M. Carpentieri, Y. Liu, Y. Guang, J. Gräfe, M. Weigand, D. M. Burn, G. van der Laan, T. Hesjedal, Z. Yan, J. Feng, C. Wan, J. Wei, X. Wang, X. Zhang, H. Xu, C. Guo, H. Wei, G. Finocchio, X. Han, G. Schütz, *Adv. Mater.* **2019**, *31*, 1807683.

[24] W. Legrand, J. Y. Chauleau, D. Maccariello, N. Reyren, S. Collin, K. Bouzehouane, N. Jaouen, V. Cros, A. Fert, *Sci. Adv.* **2018**, *4*, eaat0415.

[25] F. Ma, Y. Zhou, H. B. Braun, W. S. Lew, *Nano Lett.* **2015**, *15*, 4029.

[26] A. Roldán-Molina, A. S. Nunez, J. Fernández-Rossier, *New J. Phys.* **2016**, *18*, 045015.

[27] S. A. Díaz, J. Klinovaja, D. Loss, *Phys. Rev. Lett.* **2019**, *122*, 187203.

[28] S. K. Kim, Y. Tserkovnyak, *Phys. Rev. Lett.* **2017**, *119*, 077204.

[29] L. Sun, R. X. Cao, B. F. Miao, Z. Feng, B. You, D. Wu, W. Zhang, A. Hu, H. F. Ding, *Phys. Rev. Lett.* **2013**, *110*, 167201.

[30] S. Pu, M. Dai, G. Sun, *Opt. Commun.* **2010**, *283*, 4012.

[31] B. F. Miao, L. Sun, Y. W. Wu, X. D. Tao, X. Xiong, Y. Wen, R. X. Cao, P. Wang, D. Wu, Q. F. Zhan, B. You, J. Du, R. W. Li, H. F. Ding, *Phys. Rev. B* **2014**, *90*, 174411.

[32] J. Li, A. Tan, K. W. Moon, A. Doran, M. A. Marcus, A. T. Young, E. Arenholz, S. Ma, R. F. Yang, C. Hwang, Z. Q. Qiu, *Nat. Commun.* **2014**, *5*, 4704.

[33] D. A. Gilbert, B. B. Maranville, A. L. Balk, B. J. Kirby, P. Fischer, D. T. Pierce, J. Unguris, J. A. Borchers, K. Liu, *Nat. Commun.* **2015**, *6*, 8462.

[34] K. Y. Guslienko, *IEEE Magn. Lett.* **2015**, *6*, 4000104.

[35] H. Z. Wu, B. F. Miao, L. Sun, D. Wu, H. F. Ding, *Phys. Rev. B* **2017**, *95*, 174416.

[36] G. Chen, A. Mascaraque, A. T. N. Diaye, A. K. Schmid, *Appl. Phys. Lett.* **2015**, *106*, 242404.

[37] Y. Y. Dai, H. Wang, P. Tao, T. Yang, W. J. Ren, Z. D. Zhang, *Phys. Rev. B* **2013**, *88*, 054403.

[38] K. Cai, M. Yang, H. Ju, S. Wang, Y. Ji, B. Li, K. W. Edmonds, Y. Sheng, B. Zhang, N. Zhang, S. Liu, H. Zheng, K. Wang, *Nat. Mater.* **2017**, *16*, 712.

[39] Y. Sheng, K. W. Edmonds, X. Ma, H. Zheng, K. Wang, *Adv. Electron. Mater.* **2018**, *4*, 1800224.

[40] A. K. Nandy, N. S. Kiselev, S. Blügel, *Phys. Rev. Lett.* **2016**, *116*, 177202.

[41] Y. Cao, A. W. Rushforth, Y. Sheng, H. Zheng, K. Wang, *Adv. Funct. Mater.* **2019**, *29*, 1808104.

[42] G. Y. Shi, C. H. Wan, Y. S. Chang, F. Li, X. J. Zhou, P. X. Zhang, J. W. Cai, X. F. Han, F. Pan, C. Song, *Phys. Rev. B* **2017**, *95*, 104435.

[43] X. Zhang, Y. Zhou, M. Ezawa, *Nat. Commun.* **2016**, *7*, 10293.

[44] J. L. Grab, A. E. Rugar, D. C. Ralph, *Phys. Rev. B* **2018**, *97*, 184424.

[45] M. E. Stebliy, A. G. Kolesnikov, A. V. Davydenko, A. V. Ognev, A. S. Samardak, L. A. Chebotkevich, *J. Appl. Phys.* **2015**, *117*, 17B529.

[46] X. Zhang, W. Cai, X. Zhang, Z. Wang, Z. Li, Y. Zhang, K. Cao, N. Lei, W. Kang, Y. Zhang, H. Yu, Y. Zhou, W. Zhao, *ACS Appl. Mater. Interfaces* **2018**, *10*, 16887.

[47] Y. Li, X. Jin, P. Pang, F. N. Tan, W. S. Lew, F. Ma, *Chin. Phys. B* **2018**, *27*, 127502.

[48] L. Wang, Q. Feng, Y. Kim, R. Kim, K. H. Lee, S. D. Pollard, Y. J. Shin, H. Zhou, W. Peng, D. Lee, W. Meng, H. Yang, J. H. Han, M. Kim, Q. Lu, T. W. Noh, *Nat. Mater.* **2018**, *17*, 1087.

[49] H. Zhou, L. Wang, Y. Hou, Z. Huang, Q. Lu, W. Wu, *Nat. Commun.* **2015**, *6*, 8980.

[50] LLG Micromagnetics Simulator developed by M. R. Scheinfein, http://llgmicro.home.mindspring.com/ (accessed: December 2015).